Journal of Solid Mechanics and Materials Engineering

Vol. 6, No. 9, 2012

Strain Monitoring and Applied Load Estimation for the Development of Intelligent Tires Using a Single Wireless CCD Camera*

Ryosuke MATSUZAKI**, Naoki HIRAOKA***, Akira TODOROKI***
and Yoshihiro MIZUTANI***

** Department of Mechanical Engineering, Tokyo University of Science
2641 Yamazaki, Noda, Chiba, Japan
E-mail:rmatsuza@rs.tus.ac.jp

*** Department of Mechanical Sciences and Engineering, Tokyo Institute of Technology
2-12-1 O-okayama, Meguro, Tokyo, Japan

Abstract

From a traffic safety point of view, there is an urgent need for intelligent tires which can optimize braking control by estimating the slip ratio and friction coefficient between a road surface and an automobile tire. The present study develops concurrent monitoring of frictional and vertical loads applied to the tires from the inner tire strain data for estimating the road/tire friction coefficient, which enables optimization of vehicle control and implementation of a road condition warning system. The tire strain is obtained using a three-dimensional digital image correlation method with a single wireless CCD camera attached to the wheel rim inside the tire. The procedures of the applied load estimation decompose the measured strain into the frictional and vertical strain components using their symmetrical and anti-symmetrical characteristics. Static tire rotation tests were carried out, and the applied loads were estimated from the inner tire surface strain distribution. Compared with the actual applied loads measured from strain gages attached to the experimental apparatus, it was confirmed that the vertical and frictional loads can be estimated independently with adequate accuracy.

Key words: Automobile, Strain Monitoring, Digital Image Correlation Method, Intelligent Tires, Wireless

1. Introduction

There is an urgent need, from a traffic safety point of view, for intelligent tires [1-4] equipped with sensors for monitoring applied strain [5-7] and tire pressure monitoring systems [8-13], which are now mandatory in the United States [14, 15]. These intelligent tires are effectively improving reliability and control systems such as anti-lock braking systems [16-19]. The key factors for intelligent tire sensors are the development of direct tire deformation or strain measurements, and the demonstration of a typical model of strain data for improved safety and comfort, as well as providing additional features that can be used in other aspects of automotive safety and design [20].

For the sensors, Pohl et al. [21, 22] have showed that it is possible to monitor road surface friction utilizing the deformation of the tread elements by using SAW sensors fixed on the interior surface of tire rubber. Yilmazoglu et al. [23] used magnetic field sensors implanted in tire rubber for the detection of tread deformation. Matsuzaki et al. also developed a patch type strain sensors for

*Received 13 Feb., 2012 (No. 12-0111)
[DOI: 10.1299/jmmp.6.935]

intelligent tires based on changes in capacitance [24-26]. The sensor uses a very soft material so that it does not interfere with the tire deformation and avoids debonding. Another sensor proposed is a self-sensing method that uses the embedded steel wire in the tire itself as the sensor [27]. This has the advantage that an attached sensor is not needed and debonding problems are eliminated. However, these sensors measure only local strain are not capable of measuring momentary strain distribution. To address this issue, an optical method was developed for the concurrent monitoring of in-plane strain and out-of-plane displacement (rolling radius) [28, 29]. The optical method enables contact-less measurement of full-field strain distribution. The in-plane strain and out-of-plane displacement are calculated using a three-dimensional digital image correlation method (3D DICM) with an image of the interior surface of a tire that is taken with a single CCD camera fixed on the wheel rim, whereas conventional 3D DICM uses tomography images [30] or stereo vision [31].

The general model for the application of strain data was investigated for an optimized braking control and road condition warning system by the authors [32]. The relationship between strain sensor outputs and tire mechanical parameters, including braking torque, effective radius and contact patch length, were calculated using finite element analysis. An estimating method for the slip ratio and frictional coefficient between the road and tire surface was proposed. Here the friction coefficient μ is a key parameter indicating the braking/accelerating efficiency, and is defined by the longitudinal tire force (frictional force), F_x, divided by the normal force (wheel load), F_z: $\mu=F_x/F_z$. The road condition warning would be actuated if the recorded friction coefficient at a certain slip ratio was lower than a 'safe' reference value. However, the study only investigated the situation in which either the vertical or the frictional load changed while the other was assumed constant. Because both the frictional and vertical loads alter the strain data, an independent estimation method that separates frictional and vertical loading effects on the strain, is needed.

Our previous study [33] proposed a concurrent estimating method for frictional and vertical loads applied to a tire from the tire strain data when both loads were changing. Finite element method (FEM) analysis was used for simulating tire deformation under various wheel loads and braking torques, and the relationship between the strain distribution and the applied loads were investigated. However, the investigation was limited in the simulation analysis, and the practical model for obtaining tire strain distribution for estimating the applied load has not been constructed.

In this study, we construct a novel applied load estimation system combined with 3D DICM with a single wireless CCD camera attached to the wheel rim inside the tire as shown in figure 1. The advantage of the system is that is noncontact to tire surface, obtaining information of 3D tire deformation, compatible with wireless system, easy to install in the tire and control system, and can be performed in real-time. In this proposed system, the tire surface deformation was obtained by noncontact optical method; the data were sent wirelessly to the external equipment using a wireless transmitter; the strain distribution was calculated using 3D DICM outside the tire. Finally, the applied loads were estimated from the actual inner tire surface strain distribution to demonstrate the proposed intelligent tire. The estimation accuracy of the applied loads was investigated by comparing with the reference load obtained by the conventional strain gages attached to the experimental apparatus.

2. Strain distribution of the inner tire surface

When a tire contacts the road surface, the tread at the contact point bends, and a tensile strain distribution occurs on the inner tire surface in the circumferential direction, whereas a compressive strain occurs outside the contact patch. In this

bending, since there is friction between the road and tire surfaces, the presence of the frictional load slightly reduces the changes in the tensile strain. This strain component due to friction is compressive strain. When there is only a vertical (or wheel) load without rotational torque, a symmetrical tensile strain distribution between the front and rear of the contact patch is observed.

When the tire is rotating and a braking torque is applied, the tread deforms in a shear manner due to friction. This shear deformation creates an anti-symmetrical strain distribution to the center of the contact point. This is because the vertical load distribution has its maximum at the center of the contact point and zero at the contact edge; thus the displacement due to friction is greatest at the center and decreases to zero near the contact edge.

Therefore, the strain measured by a sensor, which is the strain in the circumferential direction, is the sum of the above three strain components (figure 2), due to:

i) Vertical loads, ε_{ver}

ii) Frictional loads when bending, ε_{flat}

iii) Frictional loads when driving/braking, ε_{fri}

In these three strains, the strains ε_{ver} and ε_{flat} are symmetrical, and it is difficult to separate them from each other. In actual tire/road conditions, ε_{flat} is much smaller than ε_{ver}; thus the measured circumferential strain ε_{cir} is assumed to be the sum of the vertical and frictional strain components as follows:

$$\varepsilon_{cir} \approx \varepsilon_{ver} + \varepsilon_{fri} . \tag{1}$$

In the measurements, the strain ε_{cir} is decomposed into the strain components of ε_{ver} and ε_{fri}; and the frictional load is estimated from the strain ε_{fri} while the vertical load is from the strain ε_{ver}.

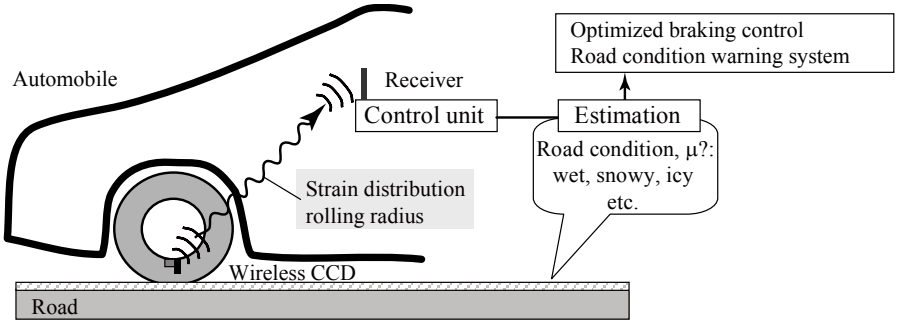

Figure 1 Diagram of intelligent tire system for monitoring road conditions based on image sensing.

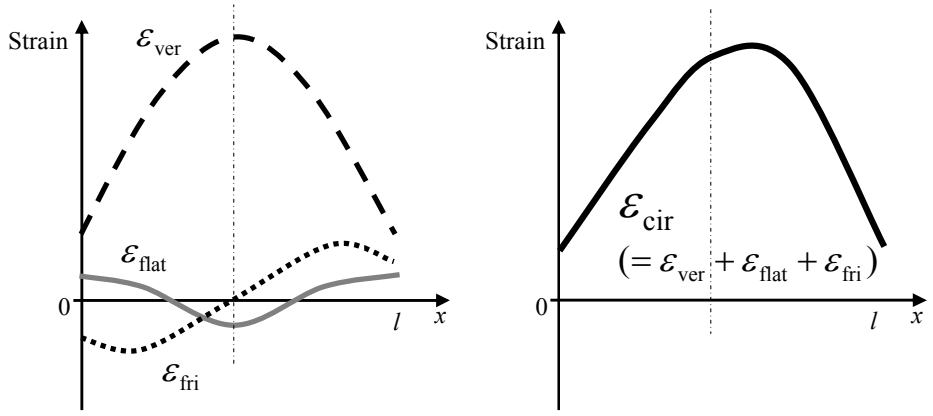

(a) (b)

Figure 2 Strain components and total strain of the circumferential strain of the inner surface of a tire: (a) strain components (b) total strain.

3. Applied load estimation

3.1 Vertical Load Parameter

The measured circumferential strain is affected by the vertical and frictional loads. Thus to estimate the vertical load independent of the frictional load, the strain due to the friction has to be removed from the circumferential strain. The deformation δ_f in the circumferential direction on the tire surface due to friction is linearly related to the frictional stress f_x with the coefficient α and expressed as

$$\delta_f = \alpha f_x . \tag{2}$$

The circumferential strain due to the friction is

$$\varepsilon_{fri} = \frac{d\delta_f}{dx} . \tag{3}$$

The frictional stress f_x at the edge of the contact patch is zero since the vertical load is zero at these points; thus the integration of the strain ε_{fri} is

$$\int_0^l \varepsilon_{fri}\, dx = \int_0^l \frac{d\delta_f}{dx} dx = [\alpha f_x]_0^l = 0 , \tag{4}$$

where the x coordinate is along the length of the contact patch; is zero at the edge, and the patch length is l. The contact patch position can be estimated by calculating the waveform of the spatial derivative of strain [34].

Since the circumferential strain ε_{cir} is the sum of ε_{ver} and ε_{fri}, the vertical load parameter $E_{vertical}$, which depends only on ε_{ver} and is independent of frictional loads, can be obtained by integrating the strain ε_{cir}

$$E_{vertical} = \int_0^l \varepsilon_{cir}\, dx = \int_0^l (\varepsilon_{ver} + \varepsilon_{fri}) dx = \int_0^l \varepsilon_{ver}\, dx . \tag{5}$$

In the actual measurement procedure, the circumferential strain ε_{cir} is measured first; then the strain is differentiated along x, and the contact patch length l is calculated. The strain distribution ε_{cir} on the contact patch is then integrated between x=[0, l], and $E_{vertical}$ is calculated from equation (5).

3.2 Frictional Load Parameter

The frictional load F_x is calculated by integrating the frictional stress f_x along the x axis, and expressed using ε_{fri} from equations (2) and (3).

$$F_x = \int_0^l f_x\, dx = \int_0^l \frac{1}{\alpha}\delta_f\, dx = \int_0^l \left\{ \frac{1}{\alpha}\int_0^x \varepsilon_{fri}(\xi) d\xi \right\} dx . \tag{6}$$

From the symmetrical and anti-symmetrical characteristics of the strains ε_{ver} and ε_{fri}, the following relationships are obtained:

$$\varepsilon_{ver}(\xi + \frac{l}{2}) = \varepsilon_{ver}(-\xi + \frac{l}{2}), \quad \varepsilon_{fri}(\xi + \frac{l}{2}) = -\varepsilon_{fri}(-\xi + \frac{l}{2}) . \tag{7}$$

From these relationships, the strain due to friction ε_{fri} can be expressed using the circumferential strain ε_{cir} as follows:

$$\varepsilon_{cir}(\xi + \frac{l}{2}) - \varepsilon_{cir}(-\xi + \frac{l}{2}) = \left\{ \varepsilon_{ver}(\xi + \frac{l}{2}) + \varepsilon_{fri}(\xi + \frac{l}{2}) \right\} - \left\{ \varepsilon_{ver}(-\xi + \frac{l}{2}) + \varepsilon_{fri}(-\xi + \frac{l}{2}) \right\} = 2\varepsilon_{fri}(\xi + \frac{l}{2}) \tag{8}$$

.

Therefore, using equations (6) and (8), the frictional force F_x can be calculated from the sensor output ε_{cir}.

When the vertical or frictional load is quite large, the deformed area becomes wider and expands outside the contact patch. In this case, the integration needs to

be done along the $\delta_f \neq 0$ area, which is larger than the contact patch or the sensing area. For practical monitoring, a method to estimate the frictional load from the strain distribution using only the contact patch area is required.

For this reason, we introduce and use the maximum deformation as

$$\delta_{\text{fmax}} = \gamma \int_0^{l/2} |\varepsilon_{\text{fri}}(x)| dx \cdot \tag{9}$$

where γ is the correction factor which neglects the widespread deformation beyond the contact patch.

For simplicity, the frictional load F_x can be evaluated using the maximum frictional stress ($f_{x\max}$) times the contact length (l) with the ratio φ as follows by rewriting equation (6):

$$F_x = \int_0^l \left\{ \frac{1}{\alpha} \int_0^x \varepsilon_{\text{fri}}(\xi) d\xi \right\} dx = \varphi l f_{x\max} = \varphi l \frac{1}{\alpha} \gamma \int_0^{l/2} |\varepsilon_{\text{fri}}(x)| dx \cdot \tag{10}$$

Therefore, the frictional load parameter E_{friction} indicating the frictional load is expressed by

$$E_{\text{friction}} = l \int_0^{l/2} |\varepsilon_{\text{fri}}(x)| dx \cdot \tag{11}$$

Here, $\varepsilon_{\text{fri}}(x)$ in equation (11) can be calculated from the ε_{cir} using equation (8). Note that the coefficients α, γ and φ are not required in the actual estimating procedures from equations (5) and (11). The applied vertical and frictional loads increase with the increase of the parameters of E_{vertical} and E_{frciton}. Since there is a small nonlinearity between the parameters and the actual loads, a polynomial regression is used to estimate the applied loads from the parameters. Using the integration of the inner tire surface, the adverse local high strain induced by a rough road surface is alleviated by the tread deformation and integration along the contact patch.

4. Strain measurements using 3D DICM

4.1 Digital Image Correlation Method

An optical method is used for the concurrent monitoring of in-plane strain and out-of-plane displacement (rolling radius) utilizing the non-planar surface of the monitored object. The optical method enables noncontact measurement of strain distribution. The in-plane strain and out-of-plane displacement are calculated using image processing with an image of the inner surface of a tire that is taken with a single CCD camera fixed on the wheel rim.

The DICM was used for measurements of the in-plane strain of the tire surface. The DICM is a method that searches the same region for images before and after deformation using digital information. The in-plane deformation image can be calculated by searching the locations in the deformed image for regions of interest (ROI) that are extracted from the image before deformation. The method enables strain measurement by correlating the position of pixels in images of the undeformed and deformed objects by maximizing the correlation coefficient R using the Newton-Raphson method:

$$R(u,v) = \frac{\sum_{x=1}^{n}\sum_{y=1}^{m} \{(F(x,y)-\overline{F})(G(x+u,y+v)-\overline{G})\}}{\sqrt{\sum_{x=1}^{n}\sum_{y=1}^{m}(F(x,y)-\overline{F})^2}\sqrt{\sum_{x=1}^{n}\sum_{y=1}^{m}(G(x+u,y+v)-\overline{G})^2}} \tag{12}$$

where F and G are gray levels of ROIs extracted from images before and after deformation, $\overline{F}$, $\overline{G}$ are average amounts of gray levels in each whole ROI, (u, v)

are the displacement values of the ROI in the x and y direction, and (n, m) are the sizes of the ROI in the x and y directions. Interpolating pixels of deformed images enables higher accuracy in the measurement of deformation occurring in images by sub-pixel pattern matching.

4.2 3-D Measurements using Non-planar Surface

The in-plane displacement occurs in the acquired image corresponding to the out-of-plane displacement dh between a camera and the measured object [35]. We define the in-plane displacement in the images including the out-of-plane displacement effect, as an apparent strain. The apparent ε' strain can be calculated as follows:

$$\varepsilon' = \frac{h_0}{h_0 + dh} - 1 \tag{13}$$

where h_0 is the initial distance between the camera and measured object. Equation (13) indicates that the apparent strain ε' also depends on h_0 and has a different value even when the same out-of-plane displacement dh occurs.

Let us consider the case of attaching a small block, whose height is l, on the measured object as shown in figure 3(a). When the distance between the camera and measured object is h, the distance between the camera and block surface is h-l. We define the actual in-plane strain as ε_1 and ε_2 in the measured object and block top surface. From equation (13), the apparent strain, which includes the actual in-plane strain and in-plane displacement corresponding to the out-of-plane displacement, of the measured object $\varepsilon_1'$and the block top surface ε_2' can be expressed using the different initial distance as follows:

$$\varepsilon_1' = \varepsilon_1 + \left(\frac{h_0}{h_0 + dh} - 1 \right) \tag{14}$$

$$\varepsilon_2' = \varepsilon_2 + \left(\frac{h_0 - l}{h_0 + dh - l} - 1 \right) \tag{15}$$

In the tire measurement, the block height l and initial distance h_0 are initially known values determined from the tire size and air pressure, and the apparent strains ε_1' and ε_2'can be measured using the DICM. Since the three quantities of ε_1, ε_2 and dh are unknown, these cannot be solved from the two equation (14) and (15). Therefore, we assume that there is some relationship between ε_2 and ε_1 since the strain distribution is nearly constant in the vicinity of one block. Because the strain ε_2 can be estimated from ε_1 using this relationship, the in-plane strain of the measured object ε_1 and the out-of-plane displacement dh can be calculated using equations (14) and (15). The calculation flow chart is summarized in figure 3(b). Since the out-of-plane displacement between blocks can also be obtained using the approximate function, the full-field in-plane deformation distribution is possible. The apparent strains ε_1' and ε_2' are calculated using numerical differentiation of the in-plane displacement obtained using the DICM.

In our case, it was confirmed by the FEM analysis that the block top surface strain ε_2 is small enough compared with the apparent strain due to out-of-plane displacement (several tens of thousands μ) or the applied in-plane strain (from −1000 to 3000 μ), from which we can approximate the strain ε_2 as zero. Therefore, in actual measurements, the measured in-plane object strain ε_1 and out-of-plane displacement dh can be obtained using the following equation:

$$dh = \frac{h_0 - l}{\varepsilon_2' + 1} - (h_0 - l) \tag{16}$$

$$\varepsilon_1 = \varepsilon_1' - \left(\frac{h_0}{h_0 + dh} - 1 \right) \tag{17}$$

The validity and the estimation accuracy of this 3-D DICM were investigated using an aluminum beam and tire surface [28]. The maximum error of the out-of-displacement measurements was 0.3 % to the shooting distance. Although the scatter of the in-plane strain measurements is about 0.02 % due to the pattern matching error, the averaging at multi-points decreases this scatter.

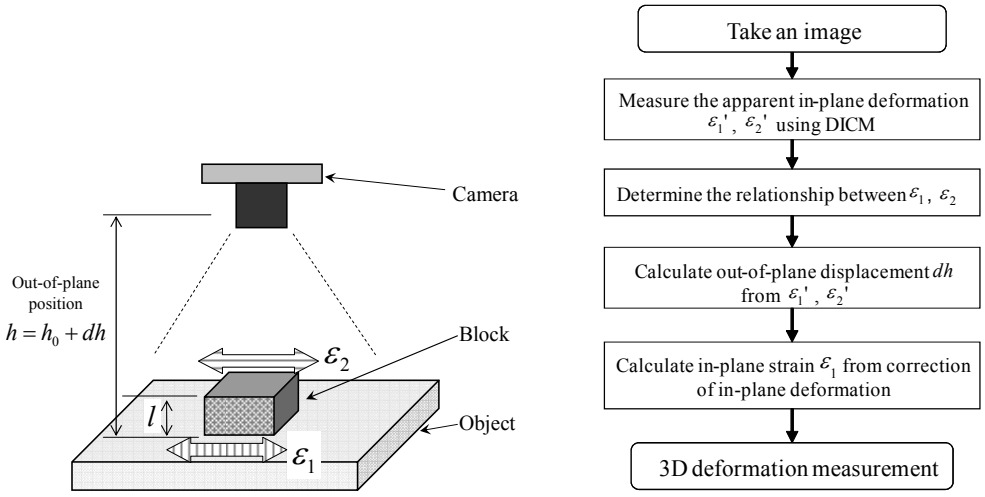

(a) (b)

Figure 3 Three-dimensional digital image correlation method using a single camera and non-planar surface: (a) schematic diagram and (b) flow chart of measurement procedures.

5. Experimental procedure

The tire used was a 17-inch radial type Bridgestone Dueler (235/65R17 104V), and the wheel was a 3-piece type of Work VS-XX (17×7.5JJ 5H-114.3). The air pressure was set to 200 kPa. For image measurements inside the tire, a wireless CCD camera (1/3 inch Sony Super HAD CCD, 640×480 pixels) was fixed to the rim inside the tire. To illuminate the tire interior, an LED was also embedded inside the tire. The image signal was wirelessly sent to an external receiver and input to an image processing unit National Instruments PXI-1411 and LabVIEW ver. 8 as shown in figure 4(a). For full-field 3D measurement using the DICM, the 14 rubber blocks (Tigers Polymer, elastic modulus 9 MPa, Poisson's ratio 0.49) were attached with a spacing of 5 mm using elastic adhesives as shown in figure 4(b). A random pattern was painted with white spray on the surface of the tires to facilitate pattern matching. The stiffness of tire structures is attributed to the embedded carcass and steel belt layer, thus the effect of attaching small blocks on the global tire deformation would be small. In the future, the convex lines originally manufactured on tire inner surface can be used instead of attaching rubber blocks.

Tire rotation tests were conducted in a static condition using a purpose built tire rotating machine. The test setup is shown in figure 5. The wheel was fixed to an alumina shaft and supported the steel columns with a shaft bearing. The vertical load was adjusted by inserting various thickness plates between the tire and bottom plate. Tire rotational torque was applied manually using a wrench at the rotation axis ends. The reference values of the applied vertical and frictional loads were

obtained from the biaxial strain gages attached to the wheel axis.

Five experiments were carried out under different conditions: the vertical load, the maximum frictional loads and the number of acquired images in each experiment are shown in table 1. Under each condition, multiple images were taken during the tire rotation with almost constant vertical load and variable frictional loads from zero to the maximum indicated in table 1.

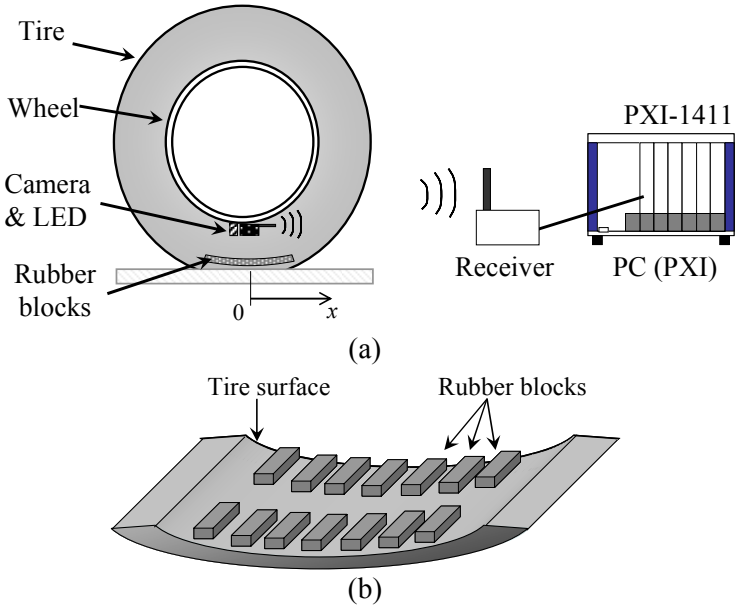

Figure 4 Experimental setup of the image measurement system of the tire: (a) set up overview and (b) inner surface of the tire.

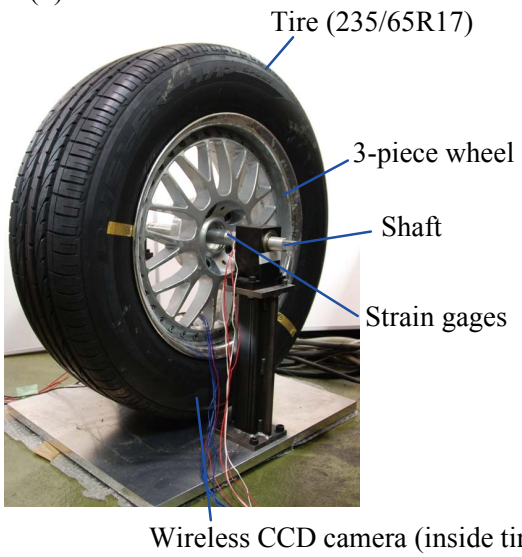

Figure 5 Apparatus setup for applying vertical and frictional loads to the automobile tire.

Table 1 Experimental conditions of vertical and frictional loading.

Experiment Number	Vertical load (N)	Maximum frictional load (N)	Number of images
Ex. 1	380	115	35
Ex. 2	607	121	32
Ex. 3	748	150	26
Ex. 4	1011	198	40
Ex. 5	1262	156	33

6. Results and discussion

6.1 Estimation of Vertical Loads

The vertical loads were estimated under the condition that both vertical and frictional loads change. Figure 6 shows the tire surface image wirelessly transmitted from the CCD camera embedded inside the tire. It can be seen from the image that the multiple rubber blocks were attached to the tire surface and random white patterns were painted on the tire surface for the 3D DICM. The in-plane strain of the bottom surface of the tires was calculated using the developed system, considering the out-of-plane displacement (rolling radius) changes. Figure 7 shows the circumferential strain when zero frictional load was applied in Ex. 1-5. The abscissa is the circumferential coordinate x: x=0 is located on the left edge of the image. Figure 8 shows the strain differentiated by x. Since it is known that the distance between the two peaks of the differentiated strain curves corresponds to the contact patch edge [34], the contact patch was located at about x=[15,50]. Therefore, around the center of the contact patch, a large tensile strain can be observed, whereas some compression exists outside the contact patch. This deformation behavior agrees well with the strain gage measurements [27] and FEM results [33].

The information from the contact patch edge was also required for calculating the applied loads in equations (5) and (11), and the calculated contact patch length in each experiment is shown in figure 9. The white bar is only the vertical load condition, and the gray is the vertical loads with maximum frictional load condition in each experiment. The contact patch length is the key parameter that changes with the road condition and is only obtained from the tire deformation measurements. Although there is a strong relationship between the vertical loads and the contact patch length, the contact patch length increased as the vertical loads increased, and the length in Ex. 4 was smaller than that in Ex. 3 which was subjected to smaller vertical loads. Considering the fact that the frictional load in Ex. 4 was the highest, the frictional load also affected the contact length.

Based on the proposed estimation procedure indicated in equation (5), the vertical load was calculated by decomposing the measured circumferential strain ε_{cir} using the symmetrical and anti-symmetrical characteristics of ε_{ver} and ε_{fri}. Figure 10 shows the actual vertical loads obtained from the strain gage attached to the experimental apparatus and the estimated vertical loads from the strain on the tire. The estimated vertical loads were calculated by approximating the relationship between $E_{vertical}$ and F_z using cubic polynomial regression. All experimental results obtained are plotted, although the results with the same vertical load and different frictional loads almost overlapped. As can be seen from the figure, the estimated vertical loads agree well with the applied load independent of the frictional loads. It was confirmed that the vertical load can be estimated within the error range of ±100 N even when the frictional loads changed their condition. The maximum error was 10.4 % in Ex. 3, and may cause a 10 % error in frictional coefficient estimation. This error was the result of the pattern matching error in the DICM; thus the accuracy will improve when using a higher resolution digital camera.

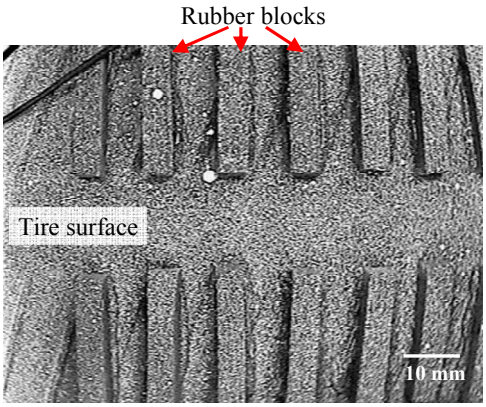

Figure 6 Image of the inner surface of the tire with rubber blocks.

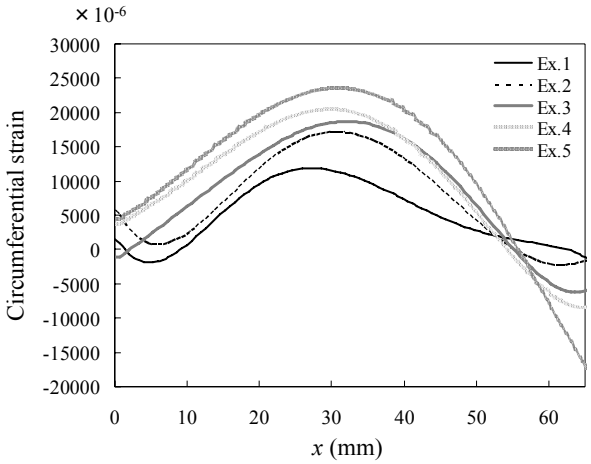

Figure 7 Circumferential strain distribution of the contact patch of the tire measured by the 3D DICM: vertical loads are from 380 to 1262 N.

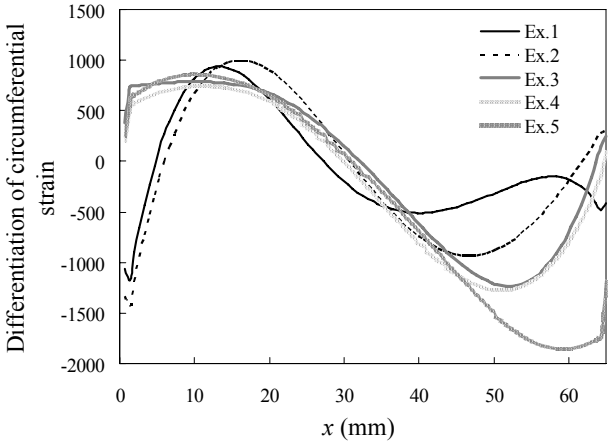

Figure 8 Differentiation of the circumferential strain of the contact patch of the tire measured by the 3D DICM: vertical loads are from 380 to 1262 N.

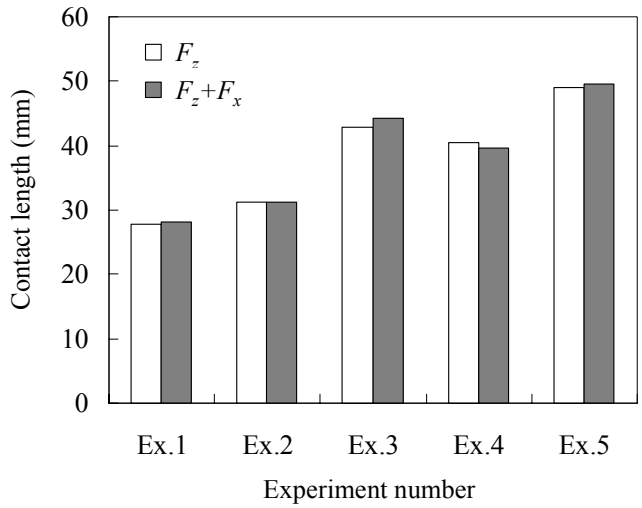

Figure 9 Contact length of the tire measured from the differentiation of circumferential strain: vertical loads are from 380 to 1262 N.

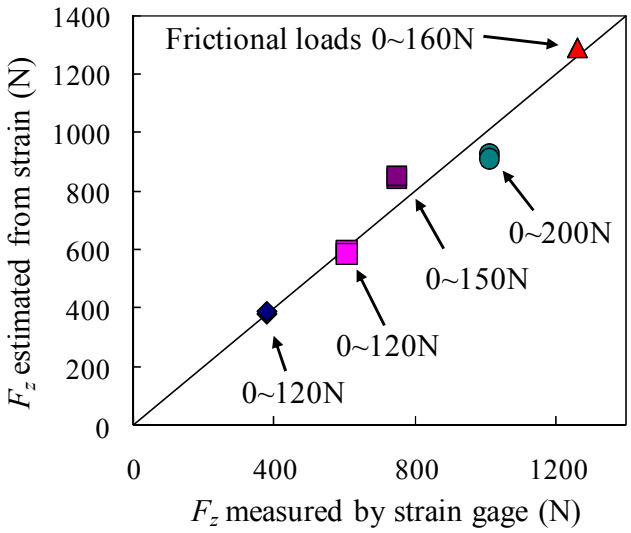

Figure 10 Estimation of the vertical load F_z using strain measurement of the tire.

6.2 Estimation of Frictional Loads

Figure 11 shows the circumferential strain ε_{cir} when the frictional load increased up to 150 N with 748 N vertical loads in Ex. 3. Figure 12 shows the frictional strain component ε_{fri} obtained by decomposing the circumferential strain. The abscissa is the circumferential coordinate x and the frictional load measured by the strain gage attached to the wheel shaft, and the ordinate is the strain on the tire surface. From figure 12, the frictional strain component is from -2000 to 1000 μ and small compared with that due to the vertical loads (from -10000 to 20000 μ). Although the strain distribution ε_{cir} seems to be symmetrical, there exists an anti-symmetrical frictional strain component, and it becomes stronger as the frictional load increases. This anti-symmetrical strain distribution due to shear deformation agrees with the frictional strain component predicted in figure 2.

As indicated in equation (11), the $E_{friction}$ is calculated for the frictional load estimation by integrating the ε_{fri} along the contact patch length, which was obtained in figure 9. Figure 13 shows the actual frictional load obtained from the strain gage

attached to the experimental apparatus and the estimated frictional loads from the tire surface strain. The estimated frictional load is calculated using linear regression from $E_{friction}$. Comparing Ex. 4 and 5, the vertical load in Ex. 5 was larger than that in Ex. 4, whereas the frictional load in Ex. 4 was larger than that in Ex. 5. The estimated results reflect this, and the frictional load can be estimated within the error of ±15 N regardless of the vertical loads. The maximum error was 10.2 % in Ex. 3, and may improve using a higher resolution digital camera as mentioned in the vertical load estimation.

From the estimation results in figures. 10 and 13, it was demonstrated that the applied vertical and frictional loads can be estimated from the tire strain measurements using the 3D DICM and decomposing the circumferential strain into frictional and vertical strain components.

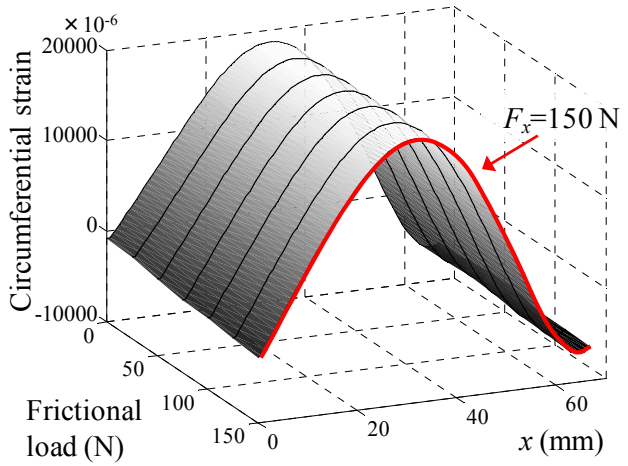

Figure 11 Circumferential strain distribution under frictional load changing: vertical load is 748 N.

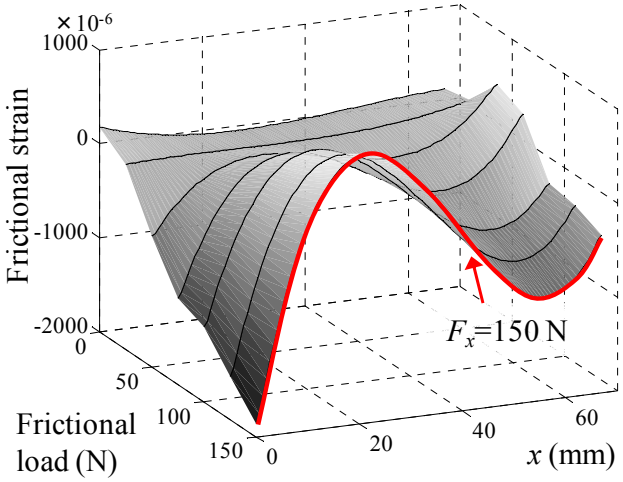

Figure 12 Frictional strain component ε_{fri} under frictional load changing: vertical load is 748 N.

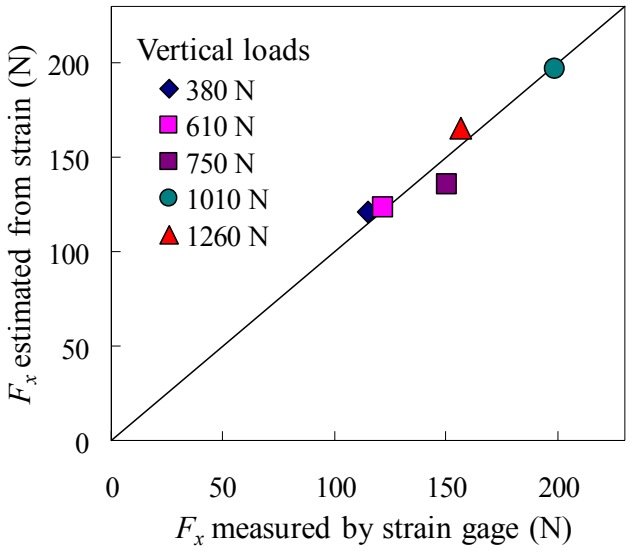

Figure 13 Estimation of the frictional load F_x using the strain measurement of the tire.

7. Concluding remarks

The validity of the applied load estimation method was experimentally investigated for the development of intelligent tires. The system developed concurrently estimates the frictional and vertical loads applied to tires from the measured strain data when both loads are changing. The estimating method decomposes the measured circumferential strain into the frictional and vertical strain components using their symmetrical and anti-symmetrical characteristics. The applied loads from the static tire rotation tests were estimated using the inner tire surface strain distribution. The tire strain distribution was obtained using a 3D DICM with a single wireless CCD camera attached to the wheel rim inside the tire. Comparing the applied loads calculated from the strain gage attached to the experimental apparatus, it was confirmed that the vertical and friction loads can be estimated to within about a 10 % error range. Using this estimating scheme, the slip slope curve during driving can be represented, which enables the optimization of vehicle control and the implementation of a road condition warning system.

Acknowledgments

We acknowledge financial support from the Bridgestone Corp. in Japan. This research is supported by a Grant-in-Aid for Young Scientists (B) 21760066 from the Japan Society for the Promotion of Science (JSPS).

References

(1) Li, L., Wang, F.-Y., and Zhou, Q., A watch in developments of intelligent tire inspection and monitoring, *Proceedings of IEEE International Conference on Vehicular Electronics and Safety*, (2005), pp.333-338.

(2) Ergen, S. C., et al., The tire as an intelligent sensor, *IEEE Transactions of Computer-Aided Design of Integrated Circuits and Systems*, Vol.28, No.7(2009), pp.941-955.

(3) Ohori, M., Ishizuka, T., Fujita, T., Masaki, N., and Suizu, Y., Fundamental study of smart tire system, *Proceedings of IEEE Intelligent Transportation Systems Conference*, (2006), pp.1519-1524.

(4) Zhang, X., Wang, Z., Li, W., He, D., and Wang, F., A fuzzy logic controller for an intelligent

tires system, *Proceedings of IEEE Intelligent Vehicles Symposium*, (2005), pp.875-881.

(5) Sergio, M., Manaresi, N., Tartagni, M., Guerrieri, R., and Canegallo, R., On road tire deformation measurement system using capacitive-resistive sensor, *Proceedings of Second IEEE International Conference on Sensors*, (2003), pp.1059-1063.

(6) Magori, V., Magori, V. R., and Seitz, N., On-line determination of tyre deformation, a novel sensor principle, *Proceedings of IEEE Ultrasonics Symposium*, (1998), pp.485-488.

(7) Sergio, M., Manaresi, N., Tartagni, M., Canegallo, R., and Guerrieri, R., On a road tire deformation measurement system using a capacitive-resistive sensor, *Smart Materials and Structures*, Vol.15, No.6(2006), pp.1700-1706.

(8) Nabipoor, M. and Majlis, B. Y., A new passive telemetry LC pressure and temperature senosr optimized for TPMS, *Journal of Physics: Conference Series*, Vol.34, (2006), pp.770-775.

(9) Kowalewski, M., Monitoring and managing tire pressure, *IEEE Potentials*, Vol.23, No.3(2004), pp.8-10.

(10) Kolle, C., et al., Ultra low-power monolithically integrated, capacitive pressure sensor for tire pressure monitoring, *Sensors*, Vol.1, (2004), pp.244-247.

(11) Yamagiwa, T., Orita, M., and Harada, T., Development of a tire pressure monitoring system for motorcycles, *JSAE Review*, Vol.23, (2003), pp.495-496.

(12) Yamamoto, S., Nakao, O., and Nishimura, H., Touch mode capacitive pressure sensor for passive tire monitoring system, *Proceedings of IEEE Sensors*, (2002), pp.1582-1586.

(13) Cullen, J. D., Arvanitis, N., Lucas, J., and Al-Shamma'a, A. I., In-field trials of a tyre pressure monitoring system based on segmented capacitance rings, *Measurement*, Vol.32, No.33(2002), pp.181-192.

(14) Title 49 United States Code 30101, Transportation Recall Enhancement, Accountability, and Documentation (TREAD) Act, Public Law 106-414-NOV.1, 106th Congress, US, (2000).

(15) National Highway Traffic Safety Administration, Federal motor vehicle safety standards; tire pressure monitoring systems; controls and displays, NHTSA-2000-8572, (2000).

(16) Palmer, M. E., Boyd, C. C., McManus, J., and Meller, S., Wireless smart tires for road friction measurement and self state determination, *Proceedings of 43rd AIAA/ASME/ASCE/AHS Structures, Structural Dynamics, and Materials Conference*, (2002), pp.AIAA-2002-1548.

(17) Todoroki, A., Miyatani, S., and Shimamura, Y., Wireless strain monitoring using electrical capacitance change of tire: part I - with oscillating circuit, *Smart Materials and Structures*, Vol.12, (2003), pp.403-409.

(18) Todoroki, A., Miyatani, S., and Shimamura, Y., Wireless strain monitoring using electrical capacitance change of tire: part II - passive, *Smart Materials and Structures*, Vol.12, (2003), pp.410-416.

(19) Li, L., Wang, F.-Y., and Zhou, Q., Integrated longitudinal and lateral tire/road friction modeling and monitoring for vehicle motion control, *IEEE Transactions on Intelligent Transportation Systems*, Vol.7, No.1(2006), pp.1-19.

(20) Matsuzaki, R. and Todoroki, A., Wireless monitoring of automobile tires for intelligent tires, *Sensors*, Vol.8, No.12(2008), pp.8123-8138.

(21) Pohl, A., Steindl, R., and Reindl, L., The "intelligent tire" utilizing passive SAW sensors - Measurement of tire friction, *IEEE Transactions on Instrumentation and Measurement*, Vol.48, No.6(1999), pp.1041-1046.

(22) Pohl, A., Ostermayer, G., Reindl, L., and Seifert, F., Monitoring the tire pressure at cars using passive SAW sensors, *Proceedings of IEEE Ultrasonics Symposium*, (1997), pp.471-174.

(23) Yilmazoglu, O., Brandt, M., Sigmund, J., Genc, E., and Hartnagel, H. L., Integrated InAs/GaSb 3D magnetic field sensors for "the intelligent tire", *Sensors and Actuators A*, Vol.94, No.1-2(2001), pp.59-63.

(24) Matsuzaki, R. and Todoroki, A., Passive wireless strain monitoring of actual tire using capacitance-resistance change and multiple spectral features, *Sensors and Actuators A*, Vol.126, No.2(2005), pp.277-286.

(25) Matsuzaki, R. and Todoroki, A., Wireless flexible capacitive sensor based on ultra-flexible epoxy resin for strain measurement of automobile tires, *Sensors and Actuators A*, Vol.140, (2007), pp.32-42.

(26) Matsuzaki, R., Keating, T., Todoroki, A., and Hiraoka, N., Rubber-based strain sensor

fabricated using photolithography for intelligent tires, *Sensors and Actuators A*, Vol.148, No.1(2008), pp.1-9.

(27) Matsuzaki, R. and Todoroki, A., Wireless strain monitoring of tires using electrical capacitance changes with an oscillating circuit, *Sensors and Actuators A*, Vol.119, No.2(2005), pp.323-331.

(28) Matsuzaki, R., Hiraoka, N., Todoroki, A., and Mizutani, Y., Optical 3D deformation measurement utilizing non-planar surface for the development of an "intelligent tire", *Journal of Solid Mechanics and Materials Engineering*, Vol.4, No.4(2010), pp.520-532.

(29) Hiraoka, N., Matsuzaki, R., and Todoroki, A., Concurrent monitoring of in-plane strain and out-of-plane displacement of tires using digital image correlation method, *Journal of Solid Mechanics and Materials Engineering*, Vol.3, No.11(2009), pp.1148-1159.

(30) Verhulp, E., Rietbergen, B. v., and Huiskes, R., A tree-dimensional digital image correlation technique for strain measurements in microstructures, *Journal of Biomechanics*, Vol.37, (2004), pp.1313-1320.

(31) Morimoto, Y. and Fujigaki, M., Automated analysis of 3-D shape and surface strain distribution of a moving object using stereo vison, *Optics and Lasers in Engineering*, Vol.18, (1993), pp.195-212.

(32) Matsuzaki, R. and Todoroki, A., Intelligent tires based on measurement of tire deformation, *Journal of Solid Mechanics and Materials Engineering*, Vol.2, No.2(2008), pp.269-280.

(33) Matsuzaki, R., Hiraoka, N., Todoroki, A., and Mizutani, Y., Analysis of Applied Load Estimation Using Strain for Intelligent Tires, *Journal of Solid Mechanics and Materials Engineering* Vol.4, No.10(2010), pp.1496-1510.

(34) Morinaga, H., Wakao, Y., Hanatsuka, Y., and Kobayashi, A., The possibility of intelligent tire (technology of contact area information sensing), *Proceedings of 31st FISITA Automotive Congress*, (2006), pp.F2006V104.

(35) Tay, C. J., Quan, C., Huang, Y. H., and Fu, Y., Digital image correlation for whole filed out-of-plane displacement measurement using a single camera, *Optics Communications*, Vol.251, (2005), pp.23-36.